ADVANCED FUNCTIONAL MATERIALS
www.afm-journal.de

Nanoflake Arrays of Lithiophilic Metal Oxides for the Ultra-Stable Anodes of Lithium-Metal Batteries

Baozhi Yu, Tao Tao, Srikanth Mateti, Shengguo Lu, and Ying Chen**

A molten lithium infusion strategy has been proposed to prepare stable Li-metal anodes to overcome the serious issues associated with dendrite formation and infinite volume change during cycling of lithium-metal batteries. Stable host materials with superior wettability of molten Li are the prerequisite. Here, it is demonstrated that a series of strong oxidizing metal oxides, including MnO_2, Co_3O_4, and SnO_2, show superior lithiophilicity due to their high chemical reactivity with Li. Composite lithium-metal anodes fabricated via melt infusion of lithium into graphene foams decorated by these metal oxide nanoflake arrays successfully control the formation and growth of Li dendrites and alleviate volume change during cycling. A resulting Li-Mn/graphene composite anode demonstrates a super-long and stable lifetime for repeated Li plating/stripping of 800 cycles at 1 mA cm^{-2} without voltage fluctuation, which is eight times longer than the normal lifespan of a bare Li foil under the same conditions. Furthermore, excellent rate capability and cyclability are realized in full-cell batteries with Li-Mn/graphene composite anodes and $LiCoO_2$ cathodes. These results show a major advancement in developing a stable Li anode for lithium-metal batteries.

1. Introduction

With the rapidly growing demand for higher energy density from industry, developing high-energy-density storage devices is imperative.[1] Lithium-metal batteries (LMBs), including Li-S batteries[2–4] and Li-air batteries,[5–7] can deliver a specific energy of ≈650 and ≈950 Wh kg^{-1}, respectively, which are 2–3 times higher than that of the current Li ion batteries, and thus are considered next-generation batteries. In both LMBs, Li-metal anode is the indispensable component because of its high theoretical specific capacity of 3860 mAh g^{-1} and the lowest redox potential (–3.04 V vs the standard hydrogen potential electrode).[8,9] However, the Li anode has two critical issues: (1) the virtually infinite relative volume change, resulting in cracks of solid–electrolyte-interface (SEI) layer;[9,10] (2) uncontrollable formation of Li dendrite during charge/discharge cycles[11,12] leading to low Coulombic efficiency, poor cyclic stability, and serious safety problems. Various strategies have been tried to regulate the undesired dendritic formation, including exploring new electrolytes and electrolyte additives,[13–15] use of solid electrolytes,[16–18] addition of artificial physical protective layers,[19,20] and design of dendrite-free current collectors.[21–24] Although these strategies can effectively suppress the formation and growth of Li dendrites, most of them fail to overcome the issue of infinite volume change originating from the hostless nature of Li-metal anode.[25]

To minimize the volume change of metallic Li, the rational design of a stable host is one of the most efficient methods.[26] 3D self-supporting interconnected carbon-based networks[27–29] could be ideal hosts. The carbon-based hosts possess high specific surface area, flexibility with light weight, stability under a redox environment, and excellent mechanical strength to accommodate volume changes.[25] Since the carbon hosts cannot be directly used in the LMBs, pre-storing Li metal in the hosts is an essential step, which greatly affects the electrochemical performance of the Li-metal anode obtained.[30] Electrodeposition is the most widely used strategy for Li pre-storing.[31–35] However, impurities and side reactions toward lithium destroy the anode during the assembly/disassembly processes.[25,26,30] Molten lithium infusion has been recently developed as a novel technique to load lithium into hosts with the advantages of homogeneous Li deposition.[25,36–38] This strategy can only be applied on the hosts that possess superior lithiophilicity and thermal stability over the melting point of lithium (180 °C). However, most carbon-based hosts are in lack of Li affinity.[25,36] Up to now, only one carbon material, reduced graphene oxide, shows good molten Li wettability.[25] Coating lithiophilic materials on the surface of the carbon-based hosts has been proposed to realize large application of molten Li infusion strategy on the carbon-based host, but only ZnO and Si have been reported to be lithiophilic materials so far.[36,37] Exploring new lithiophilic materials and a new surface functionalization strategy are of significant importance to the broader application of the molten Li infusion and the carbon-based hosts for stable Li-metal anodes.

Here, we demonstrate that a series of strong oxidizing metal oxide nanoflakes, such as MnO_2, Co_3O_4, and SnO_2, are new

Dr. B. Z. Yu, Dr. T. Tao, Prof. S. G. Lu
School of Materials and Energy
Guangdong University of Technology
Guangzhou 510006, P. R. China
E-mail: taotao@gdut.edu.cn
Dr. B. Z. Yu, Dr. S. Mateti, Dr. T. Tao, Prof. Y. Chen
Institute for Frontier Materials
Deakin University
75 Pigdons Road, Waurn Ponds, VIC 3216, Australia
E-mail: ian.chen@deakin.edu.au
The ORCID identification number(s) for the author(s) of this article can be found under https://doi.org/10.1002/adfm.201803023.

DOI: 10.1002/adfm.201803023

© 2018 WILEY-VCH Verlag GmbH & Co. KGaA, Weinheim

lithiophilic materials. The surface of graphene foams (GFs) decorated with the metal oxide nanoflakes achieve an excellent wettability of molten Li, ensuring an efficient melt infusion process of Li and strong bonding between the host and the Li metal. In addition, the nanoscale network of oxide nanoflakes decorated on the host surface provides many small 'open cages,' which divide the Li layer into many small and separate pieces, and thus effectively reduce the level of total volume change of Li-metal anode during cycling.[38,39] The metal oxide nanoflake-decorated GFs have several attractive features, including high porosity, high conductivity, and good mechanical flexibility, which are favorable for controlling dendrite growth, diminishing the volume change, stabilizing SEI, and achieving a high energy density. Based on the above novel designs and advantages, the Li-Mn/G foam anode obtained shows long-term cycling stability and flat voltage profiles with low polarization for over 800 cycles at a current density of 1 mA cm^{-2} and 300 cycles at a current density of 2 mA cm^{-2} in a symmetric cell. A full-cell battery with a $LiCoO_2$ cathode further exhibits improved rate capability and cyclability. This is a major step toward developing a stable Li anode for high-energy-density LMBs.

2. Results and Discussion

2.1. Decoration of the Hosts and Fabrication of the Composite Li Anodes

Figure 1 illustrates the fabrication process of the composite Li-metal anodes. First, the GF was synthesized via a typical chemical vapor deposition (CVD) process.[27] The graphene sheets were seamlessly interconnected into a porous and flexible 3D network (Figure S1, Supporting Information). Second, nanoflake arrays of lithiophilic metal oxides (LMONA), including MnO_2, Co_3O_4, and SnO_2, were fabricated on the GF surface via a hydrothermal process. When the metal oxide nanoflake/GF obtained was put into contact with the molten Li, Li liquid steadily seeped into, and finally filled, the whole foam. The black foams changed to bright silver because of the infusion of Li spreading all over the foam, further indicating that the whole foam can be wetted by the metallic Li. The areal mass loading of Li in the composite anode (Li-Mn/G foam) can reach 4 mg cm^{-2}, and its weight percentage in the foam is 80%. A smaller mass loading of ≈1 mg cm^{-2} was used for preparing MnO_2/G foam anodes, ensuring Li coated only on the surface of MnO_2/G foam and not got into the pore space of the foam. The influence of MnO_2 nanoflakes on the performance of Li-MnO_2/G foam anode can be clarified.

The morphology and structure of metal oxide (MnO_2, Co_3O_4, and SnO_2) nanoflake array/G foams and the resulting Li-coated foams are shown in **Figure 2**; a highly porous microstructure of the GF was still maintained after metal oxide coating (Figure 2a–c). These nanoflake array/G foams have the similar morphology. The metal oxide nanoflakes were homogenously grown on graphene backbones, and many of them stand vertically on the GF surface. These nanoflakes have the vertical height of ≈2 µm and thickness of ≈10 nm. A transmission electron microscopy (TEM) image in Figure 2d shows an inter-distance of parallel fringes of ≈7.02 Å, corresponding to the lattice spacing of birnessite-MnO_2 (0 0 1) planes. The inter-distance of

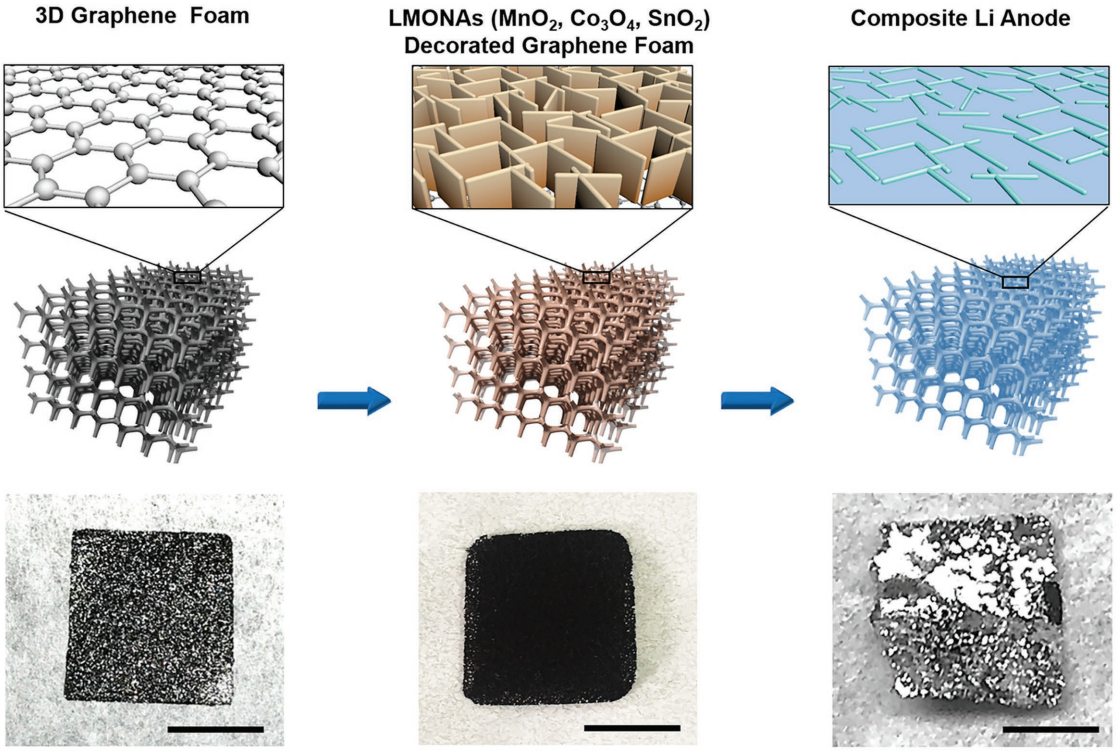

Figure 1. Schematic of the material design and the consequent synthetic procedures, and corresponding digital camera images of the GF (left), MnO_2/G foam (middle), and Li-Mn/G foam (right). The scale bar in the optical images is 1 cm.

© 2018 WILEY-VCH Verlag GmbH & Co. KGaA, Weinheim

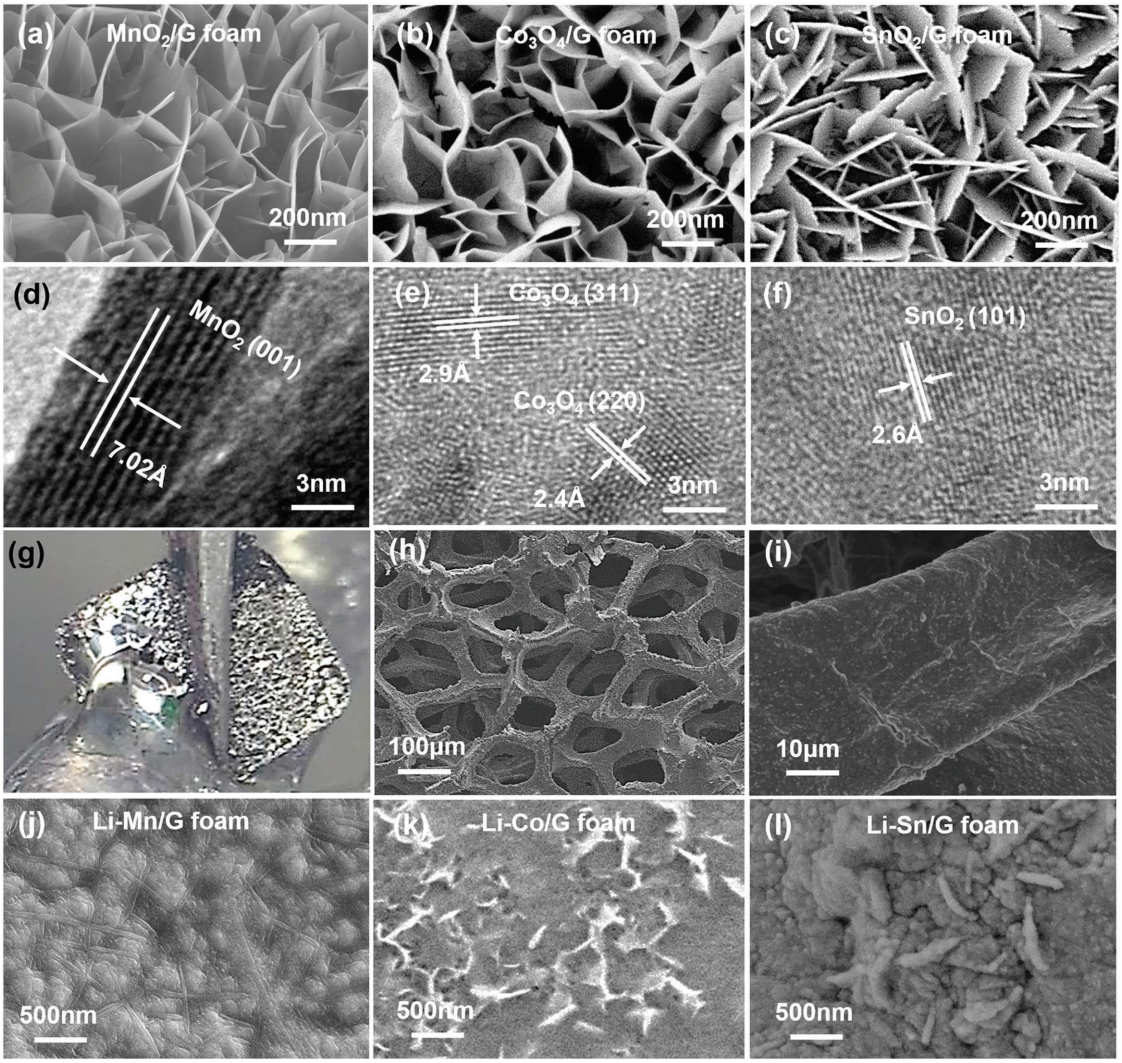

Figure 2. a–c) The SEM images and d–f) TEM images of the MnO_2/G, Co_3O_4/G, and SnO_2/G foam. g) The digital camera images of MnO_2/G foam after contacting with molten Li. h,i) The low SEM images of Li composite anodes, high-magnification SEM images of j) Li-Mn/G, k) Li-Co/G, and l) Li-Sn/G.

parallel fringes of ≈2.9 Å corresponds to the lattice spacing of Co_3O_4 (3 1 1) planes (Figure 2e), and the inter-distance of parallel fringes of ≈2.9 Å correspond to the lattice spacing of SnO_2 (1 0 1) planes shown in Figure 2f.

A sequence of time-lapse images on the infusion process of liquid Li into the metal oxide/G foam is shown in Figure 2g and Figures S5 and S6 (Supporting Information). When the black foam edge was placed in contact with the silver-colored molten Li, the Li was drawn quickly into the whole foam, which turned a silver color. One corner of the foam became silver within just 4 s and half of the black foam became shiny after 8 s. The whole infusion process took only 12 s for a large foam of 1.5 × 1.5 cm^2, which can be seen from Video S1 (Supporting Information). The fast infusion of Li liquid indicates an excellent wettability of the metal oxide/G foams. After the Li thermal infusion, 3D porous architectures of metal oxide/G foams were well preserved (Figure 2h), but the surface of the metal oxide–coated graphene backbones became smooth (Figure 2i) and the free-standing metal oxide flakes cannot be seen. High-magnification scanning electron microscopy (SEM) images (Figure 2j–l) show that Li fills the inner space between each single nanoflake. The embedded Li is completely confined within the metal oxide flakes network.

2.2. The Mechanism of Molten Li Infusion in the LMONAs

X-ray diffraction (XRD) was employed to understand the compositional evolution of the hybrid foam before and after Li coating (**Figure 3**a–c; Figure S4, Supporting Information). XRD patterns of the final foams show strong Li diffraction peaks, indicating the high loading ratio of Li. The presence of the diffraction peaks of Li_2O and Mn (Figure 3a), Li–Sn alloy ($Li_{22}Sn_5$) (Figure 3b), or Li_2O and Co (Figure 3c) indicates that the redox reaction took place between MnO_2, SnO_2, or Co_3O_4 and molten Li.

To verify the role of the oxide coating, various oxides or oxide-coated GF including MnO_2, Co_3O_4, SnO_2, NiO, CuO, and

© 2018 WILEY-VCH Verlag GmbH & Co. KGaA, Weinheim

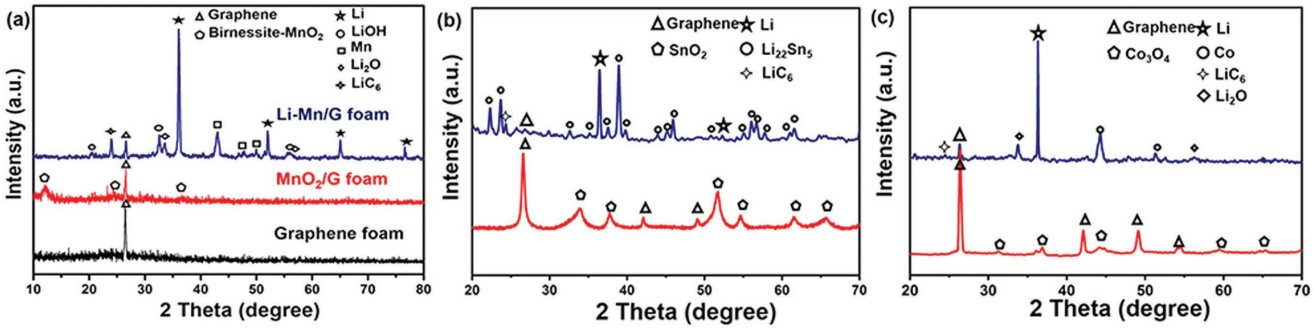

Figure 3. The XRD patterns of a) GF, MnO_2/G, and Li-Mn/G, b) SnO_2/G and Li-Sn/G, and c) Co_3O_4/G and Li-Co/G foam.

FeO were tested under the same condition (Figures S5 and S8, Supporting Information). Violent redox reaction took place between the disks of compacted commercial powders (MnO_2, Co_3O_4, and SnO_2) and molten Li (Figure S8, Supporting Information). In contrast, no reaction or infusion was observed for pure GF, compacted commercial CuO powders, compacted commercial FeO powders, or NiO nanoflake-coated GFs. These suggest that molten Li could not wet their surface (Figure S2c, Supporting Information). Therefore, the results above indicate that the MnO_2, Co_3O_4, and SnO_2 nanoflake-coated GFs have a good molten Li wettability. Compared with NiO, CuO, and FeO, MnO_2, Co_3O_4, or SnO_2 can react with molten Li more easily because the free energy change ΔG of the reaction between MnO_2 (–154 kcal), Co_3O_4 (–342 kcal), or SnO_2 (–142 kcal) and Li at 180 °C is much lower than those of NiO (–82 kcal), CuO (–102 kcal), and FeO (–73 kcal) (**Table 1**). It seems that chemical reactions between metal oxides and molten Li are a critical factor in causing the molten Li infusion. The capillarity produced by the 3D network could be another key factor to guide molten Li to fill the network. Due to the synergetic effects, molten Li can quickly wet the surface of foam and fill the porous structure. In the cases of pure GF, compacted commercial CuO powders, compacted commercial FeO powders, NiO nanoflake-coated GF, or CoO nanoflake-coated GF, there was no chemical reaction and NiO nanoflake-coated GFs have a poor Li wettability. Therefore, the chemical reaction between coating layer and molten Li can change the Li wettability of the GF, and result in the molten Li infusion. We suggest that other materials with strong oxidation that can have chemical reactions with Li may be potential candidates as a lithiophilic coating layer.

MnO_2/G foam was taken as an example to investigate the Li infusion mechanism of LMONA-decorated GF. The corresponding time-dependent evolution of morphology has been investigated to reveal the infusion process of Li in the MnO_2/G foam (**Figure 4**a,b). Obviously, the surface morphology is affected by the Li infusion time. With the continuous inflow of molten Li into the porous network, the pores begin to disappear and the surface roughness of foam obviously decreases. It is believed that both chemical reaction and physical absorption are involved during the flexible and binder-free composite lithium-metal anode. The layered birnessite-MnO_2 nanoflakes ($K_{0.46}Mn_2O_4 \cdot (H_2O)_{1.4}$) contain some solid water, which was confirmed by Fourier transform infrared spectroscopy (FTIR; Figure S9b, Supporting Information), XRD (Figure S4a, Supporting Information), and thermal gravimetric analysis (TGA; Figure S9c, Supporting Information). Both MnO_2 and H_2O could take part in the chemical reactions to form a strong bonding between the surface of nanoflakes and molten Li, but MnO_2 is primary, which is illustrated in Figure 4c. H_2O can react with molten Li to produce LiOH and hydrogen, and MnO_2 can react with molten Li to form Mn and Li_2O, as shown in the following reactions:

$$2Li + 2H_2O \rightarrow 2LiOH + H_2 \uparrow \quad (1)$$

$$MnO_2 + 4Li \rightarrow Mn + 2Li_2O \quad (2)$$

Based on the analysis above, the LMONA/G foam is an ideal host for Li infusion, and the final composite Li anode has several notable advantages as anode: (1) nanoflakes act as a lithiophilic layer to efficiently contribute to the uniform distribution of the Li in the anode. (2) The good electrical conductivity of GF enables fast electron/ion transport during Li stripping/plating. (3) The 3D network provides a stable framework and a large surface area, which are favorable to confine Li within the matrix and realize minimum volume change during Li deposition/dissolution cycling.

Table 1. The calculated ΔG of the reactions between metal oxides and molten Li.

Materials	MnO_2	Co_3O_4	SnO_2	NiO	CuO	FeO
ΔG (180 °C) (kcal)	–154	–342	–142	–82	–102	–73
Violent redox reaction	✓	✓	✓	×	×	×

2.3. Electrochemical Testing of Composite Li Anodes

The galvanostatic cycling performance of the Li-Mn/G foam anode is investigated by assembling symmetrical coin cells, and the fresh Li foil is used as the control (**Figure 5**a,b). The symmetrical cell of Li-Mn/G foam presents a low-voltage hysteresis of ≈96 mV in the initial cycle, and cycles stably over 800 cycles (1600 h) at a current density of 1 mA cm^{-2}. In contrast, the symmetrical cell of pure Li electrode shows a large voltage hysteresis (about 100 mV), its fluctuating voltage profile is clearly irregular, and voltage hysteresis increases considerably

© 2018 WILEY-VCH Verlag GmbH & Co. KGaA, Weinheim

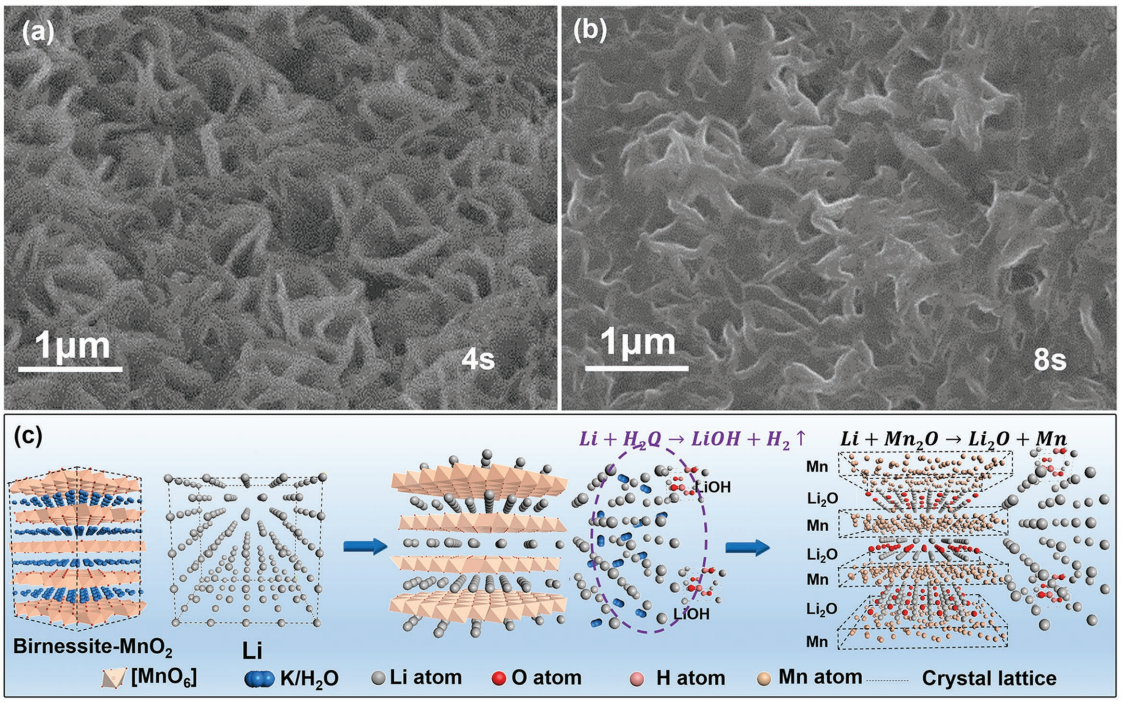

Figure 4. Top-view SEM images of the foam wetted by molten Li for different periods of time: a) 4 s, b) 8 s, and c) the schematic illustration of chemical reactions between the birnessite-MnO_2 and the molten Li.

with increasing cycle time. The 1st, 100th, 200th, and 800th cycles of the Li-Mn/G foam cells are enlarged as the insets between Figure 5a,b, further indicating that the Li-Mn/G foam can maintain stable cycling without significant increases in hysteresis. As the current density is increased to 2 mA cm^{-2}, the Li-Mn/G foam cell still maintains a very stable cycling with stable hysteresis for over 300 cycles (300 h), while the pure Li electrode cell exhibits gradual rise in voltage hysteresis. For bare Li electrodes, the severe changes in voltage at both the initial and final stages of each stripping/plating process can be ascribed to the continuous breaking and building up of SEI, followed by a dendrite-induced short-circuit. The Coulombic efficiency of cells with the GF and the MnO_2/G foam is shown in Figure 5c. The Coulombic efficiency refers to the ratio of the amount of Li stripping versus the amount of Li plating. A host (MnO_2/G foam or GF) and Li foil are assembled into a cell. In each cell test, the charge time is regulated by fixing the amount of Li depositing for 1.0 mA h cm^{-2}, and the discharge process is controlled by a cutoff voltage at 1.0 V. Detailed calculation process of Coulombic efficiency can be found elsewhere.[40,41] The Coulombic efficiency of cells with the MnO_2/G foam could maintain around 98.9% for 100 cycles at 1.0 mA cm^{-2}, while the Coulombic efficiency of cells with GF (45% after 90 cycles) is much lower than that of the MnO_2/G foam.

The top surface morphology of the Li-Mn/G foam after multiple cycles at a current density of 2 mA cm^{-2} is examined with SEM, and compared with that of the bare Li electrode (**Figure 6**). After 300 cycles, the surface of the Li-Mn/G foam remains flat without observable Li dendrites. Moreover, it is observed that the nanoflakes with integral structure uniformly disperse in the surface of the electrode (Figure 6b,d). In contrast, the surface of the bare Li electrode shows a typical Li dendritic morphology with random arrangement after 50 cycles (Figure 6a,c). The formation and growth of lithium dendrite can result in continuous consumption of electrolyte and fresh Li, and finally cause the depletion of electrolyte and the collapse of electrodes. These results suggest that the 3D porous network of the Li-Mn/G foam electrode is a relatively compact and stable configuration, which can provide a space for Li deposition and act as the ideal host to confine Li volume expansion and suppress the dendritic growth during cycling. The electrochemical impedance spectroscopy (EIS) analysis is conducted in symmetric cells before cycling, after the first cycle and 10 cycles to explore the stability of interfacial transporting behavior (Figure 6e,f). The corresponding Nyquist plots are employed to compare the internal resistances of pure Li anode and Li-Mn/G foam anode at different cycles. The semicircle at high-frequency range is associated with the interfacial resistance between electrode/electrolyte and the charge transfer resistance at the Li surface. An interfacial resistance of pure Li anode is large (≈380 Ω) before cycling (Figure 6e), which could be because of the formation of native oxide layers on the electrodes. After the first cycle, its interfacial resistance drops to 125 Ω, and to 90 Ω after 10 cycles. With the increase of charge cycles, the initial surface layer of Li anode (native oxide surface film plus SEI) cracks; the exposed 'fresh' Li generates an electrical field and new surface area. As a consequence, the interface area between the anode and the electrolyte increases, leading to a decrease of surface current density.[29,43] Besides, the native surface oxide film is broken and new surface film is incompletely formed, resulting in the decrease of overall surface resistance $R_{surface}$ and the overpotential of lithium

© 2018 WILEY-VCH Verlag GmbH & Co. KGaA, Weinheim

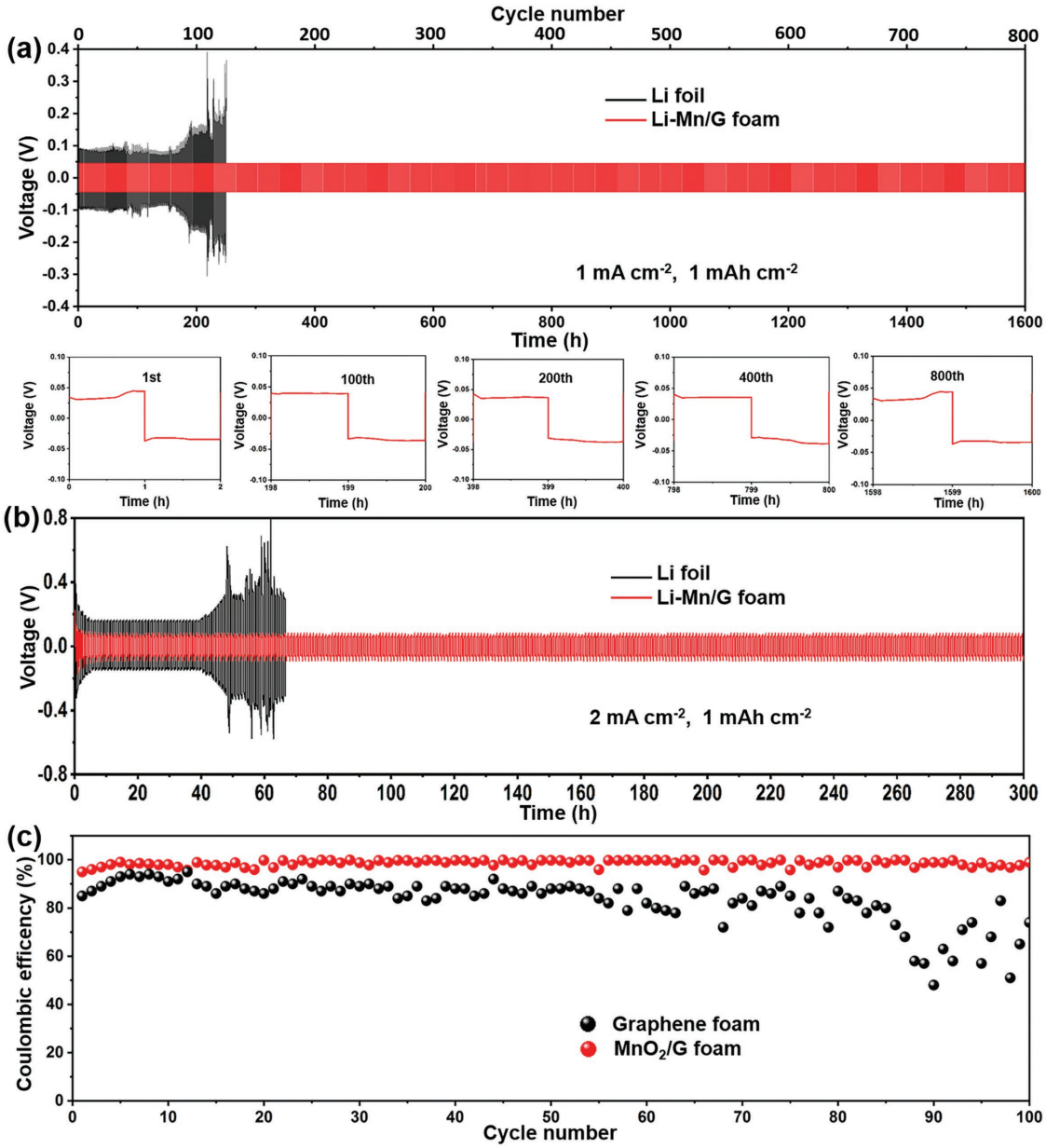

Figure 5. Long-term cycling performance of a symmetric Li-Mn/G foam (red) and bare Li foil (black) with a stripping/plating capacity of 1 mAh cm^{-2} at a) 1 mA cm^{-2} and b) 2 mA cm^{-2}. Insets, detailed voltage profiles of the 1st, 100th, 200th, 400th, and 800th cycles, respectively. c) Coulombic efficiencies of the cells with MnO_2/G foam (red) and bare GF (black) measured at 1 mA cm^{-2}.

deposition.[24,25,42,43] The significant decrease of the interfacial resistance of Li foil electrode, as shown in the EIS results, indicates unstable Li-metal anodes, while much smaller change of the interfacial resistance for the Li-Mn/G anode before and after cycling proves a better cycling stability.

In comparison, the interfacial resistance of Li-Mn/GF anode is 35 Ω before cycling, 30 Ω after the first cycle, and 28 Ω after 10 cycles, which is much lower than that of pure Li anode. Apparently, Li-Mn/GF electrodes have higher conductivity, smaller hysteresis, better architectural stability, and better Li stripping/plating kinetics than the pure Li anode.

The cycling and rate performance of the full cells of Li-Mn/GF anode directly paired with a commercial $LiCoO_2$ cathode (LCO) are shown in **Figure 7**. Compared with the similar full cell with bare Li-metal anode, the full cell with Li-Mn/GF anode exhibits a better rate capability (Figure 7a). Especially at high cycling rates, a much higher capacity for the cells with Li-Mn/GF anode can be retained (116 mAh g^{-1} at a current rate of 4 C, 1C = 120 mA g^{-1}), whereas the cells with bare Li-metal anode only deliver a capacity of 91 mAh g^{-1} at 4 C. Figure 7b compares the discharge–charge cycling stability of the cells with Li-Mn/GF anode and the cells with bare Li-metal anode. The cells with Li-Mn/GF anode deliver a specific capacity of 130 mAh g^{-1} at 1 C, and its capacity retention is 80% after 600 cycles, while the discharge capacity of the cell with bare Li-metal anode is 51 mAh g^{-1} (41% of the initial discharge capacity) after

© 2018 WILEY-VCH Verlag GmbH & Co. KGaA, Weinheim

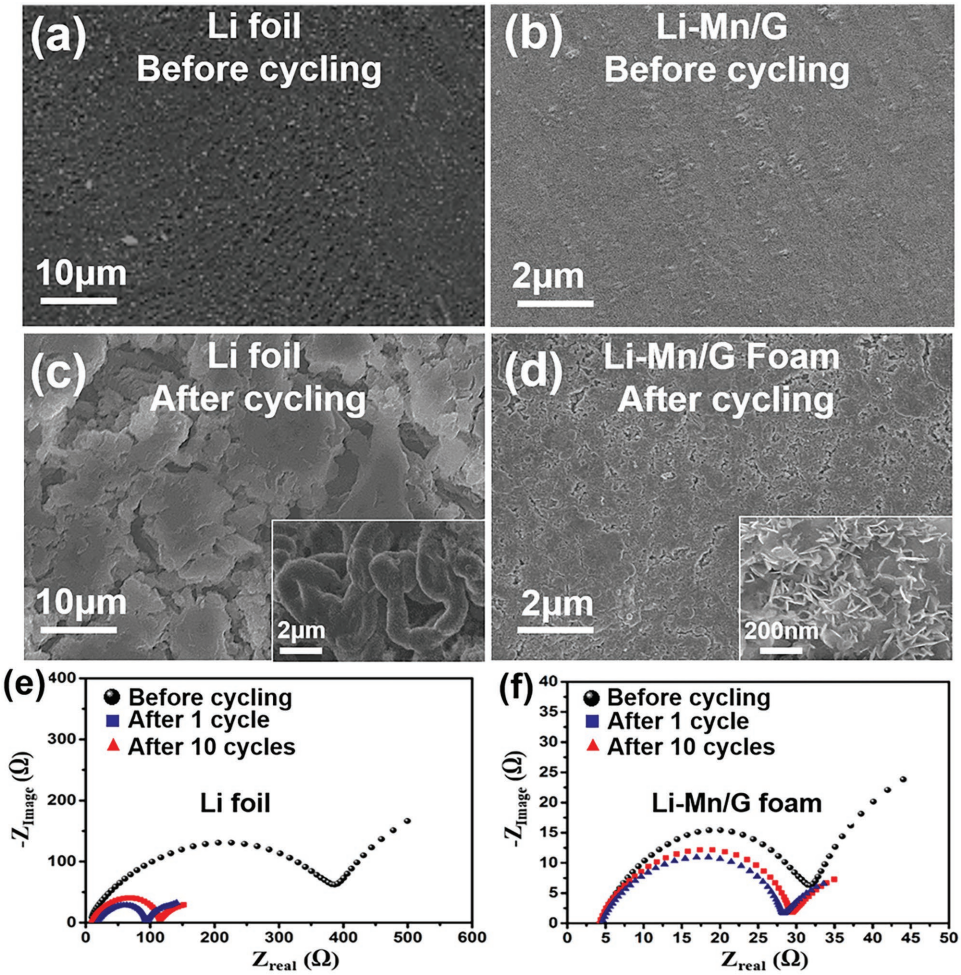

Figure 6. Top-view SEM images of a,c) the Li foil before and after cycling for 50 cycles and b,d) Li-Mn/G foam before and after cycling for 300 cycles at 2 mA cm^{-2}. e,f) Nyquist plot of the impedance spectra of the Li foil and the Li-Mn/G foam symmetric cells before and after the first and 10 galvanostatic cycles.

600 cycles. These results further confirm the superior capability of Li-Mn/GF anode working under high current densities.

This unique design of the LMONA-decorated GF has the following merits which make it such an excellent host for Li-metal anode. The ultra-strong lithiophilic nature of the metal oxides provides a strong bonding between the host surface and Li, which contributes to the uniform distribution of Li in the anode.[25,36,37] The large surface area of the anode can significantly reduce the effective current density and provides a low Li nucleation barrier during cycling as revealed by the flat stripping/plating voltage profile of the Li-Mn/G foam anode (Figure 5). According to Sand's law, the small current density consequently delays the dendrite nucleation.[39,40] In addition, the lower current density in the anode minimizes electrolyte decomposition and related SEI formation during cycling. Furthermore, the high surface energy of LMONAs makes the electron/ion highly concentrate on the nanoflakes during the stripping/plating process, according to the surface energy model.[38] The network of the nanoflake arrays acts as many open cages which suppress the volume change of the Li significantly and achieves a dendrite-free surface.

3. Conclusion

A series of novel Li composite anodes have been fabricated based on metal oxide nanoflake-decorated GFs. MnO_2, Co_3O_4, or SnO_2 are found to have an excellent affinity to molten Li, and thus contribute greatly to the fast infusion of the molten Li into the GF. The outstanding mechanical property, thermal stability, and chemical stability of metal oxide/G foam hosts ensure the structural integrity during cycling. In addition, the 3D network acts as the cages to effectively confine lithium, realize minimum volume change, stabilize electrolyte/electrode interface, and effectively suppress large dendrite formation during cycling. In comparison with the pure Li-metal anode, the Li-Mn/G foam anode shows a substantially improved performance with a long cycle life of 800 cycles and a stable voltage profile, and low hysteresis both in symmetric cells and full cells. The exploration of metal oxides as the new lithiophilic materials promotes the application of the molten Li infusion process greatly, which opens up new strategies in the construction of stable Li anodes for LMBs.

© 2018 WILEY-VCH Verlag GmbH & Co. KGaA, Weinheim

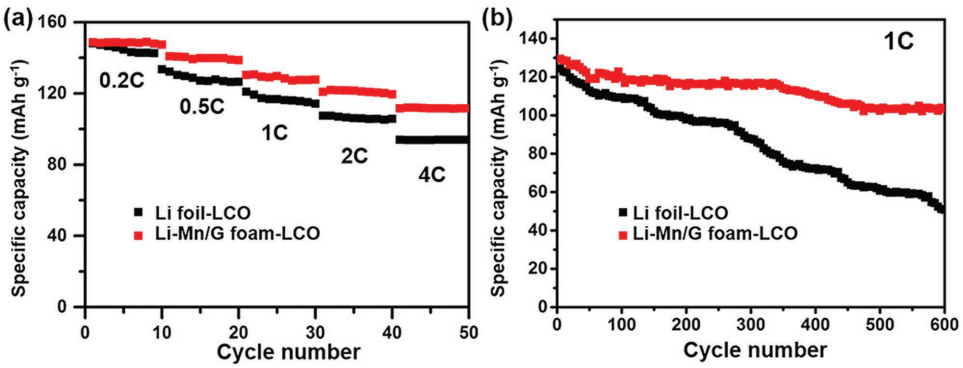

Figure 7. a) The rate capability of Li-Mn/GF-LCO cell and Li foil-LCO at various rates from 0.2 C to 4 C. b) The cycling performance of Li-Mn/GF-LCO cell and Li foil-LCO at 1 C (120 mA g^{-1}).

4. Experimental Section

*Synthesis of Metal Oxide Nanoflakes/*GFs: The GFs were synthesized via a typical chemical vapor deposition method.[27] The GFs were used as the substrates to fabricate metal oxide/G foams via a hydrothermal treatment. The details can be found in the Supporting Information.

Synthesis of Composite Li Anodes: The Li melt infusion process was performed in an argon-filled glovebox. In a typical process, the edge of a composite foam (MnO_2/G foam, SnO_2/G foam, and Co_3O_4/G foam) was placed on the surface of molten Li made by heating fresh Li foil on a hotplate, and subsequently, easily wetted and filled by molten Li in a very short time, forming the final composite Li-metal anodes. The mass loading of Li in the composite anodes can be controlled by adjusting the infusion time.

Characterizations: The morphologies of the samples were characterized with a FE-SEM Hitachi s-8600 microscope and a TEM (FEI Tecnai G2 F20) instrument. The D8 Advance X-ray diffractometer (Bruker) was used to conduct XRD. The samples were covered with Kapton tape on the holder during XRD measurements to avoid direct contact with air. A Raman microscopy system (WITec Alpha-500) with a 785 nm laser excitation source was used for the measurement of Raman spectra. FTIR spectra were recorded on a Nicolet 6700 FT-IR Spectrometer (Thermo Scientific). X-ray photoelectron spectra were determined by an X-ray photoelectron spectrometer (ESCALab MKII) with an excitation source of Mg KR radiation (1253.6 eV). TGA was performed on a NETZSCH TG 209F1 Libra (NETZSCH) instrument.

Electrochemistry Measurements: To investigate the lithium stripping/plating process, coin cells in a symmetric cell configuration were assembled with either Li-Mn/G anodes (the mass loading of Li was 1 mg cm^{-2}) or the Li foils. The 1 M lithium-bis(trifluoromethanesulfonyl) imide in 1:1 w/w 1,3-dioxolane/dimethoxyethane with 1 wt% lithium nitrate was used as the electrolyte. Celgard 2400 was used as the separator. Furthermore, galvanostatic cycling was conducted on a LAND 8-channel battery tester. For the galvanostatic cycling test in symmetrical cells, the capacities of cells were controlled at 1 mAh cm^{-2} and the cells were cycled at current densities of 1 and 2 mA cm^{-2}. The CHI 660E electrochemical workstation was used to conduct the EIS measurements.

For preparing $LiCoO_2$ cathodes, $LiCoO_2$, polyvinylidene fluoride, and carbon black were mixed with a ratio of 8:1:1. *N*-methyl-2-pyrrolidone was used as the solvent. The mass loading of cathodes was about 2.5 mg cm^{-2}. The electrolytes employed were 1 M $LiPF_6$ in a mixture of ethylene carbonate, diethyl carbonate, and dimethyl carbonate (1:1:1, by volume). The cells were galvanostatically cycled between 2.75 and 4.2 V at 1 C.

Supporting Information

Supporting Information is available from the Wiley Online Library or from the author.

Acknowledgements

The authors acknowledge the financial support from Science and Technology Planning Project of Guangdong Province, China (grant no. 2016A010104014), the Science and Technology Program of Guangzhou, China (grant no. 201607010110), Chinese Nature Science Foundation NSFC (51420105002), Chinese Postdoctoral Science Foundation (Grant No: 2017M622626), as well as the Discovery and Linkage programs awarded by the Australian Research Council.

Conflict of Interest

The authors declare no conflict of interest.

Keywords

dendrites-free batteries, lithiophilic metal oxides, lithium affinity, lithium-metal anodes, lithium-metal batteries

Received: May 2, 2018
Revised: June 21, 2018
Published online: July 27, 2018

[1] R. Bouchet, *Nat. Nanotechnol.* **2014**, *9*, 572.
[2] P. G. Bruce, S. A. Freunberger, L. J. Hardwick, J.-M. Tarascon, *Nat. Mater.* **2012**, *11*, 19.
[3] A. Manthiram, S. H. Chung, C. Zu, *Adv. Mater.* **2015**, *27*, 1980.
[4] M. Wild, L. O'Neill, T. Zhang, R. Purkayastha, G. Minton, M. Marinescu, G. Offer, *Energy Environ. Sci.* **2015**, *8*, 3477.
[5] G. Girishkumar, B. McCloskey, A. Luntz, S. Swanson, W. Wilcke, *J. Phys. Chem. Lett.* **2010**, *1*, 2193.
[6] Z. Peng, S. A. Freunberger, Y. Chen, P. G. Bruce, *Science* **2012**, *337*, 563.
[7] H. G. Jung, J. Hassoun, J. B. Park, Y.-K. Sun, B. Scrosati, *Nat. Chem.* **2012**, *4*, 579.
[8] H. Kim, G. Jeong, Y.-U. Kim, J.-H. Kim, C.-M. Park, H.-J. Sohn, *Chem. Soc. Rev.* **2013**, *42*, 9011.
[9] W. Xu, J. Wang, F. Ding, X. Chen, E. Nasybulin, Y. Zhang, J.-G. Zhang, *Energy Environ. Sci.* **2014**, *7*, 513.
[10] K. N. Wood, M. Noked, N. P. Dasgupta, *ACS Energy Lett.* **2017**, *2*, 664.
[11] R. Bhattacharyya, B. Key, H. Chen, A. S. Best, A. F. Hollenkamp, C. P. Grey, *Nat. Mater.* **2010**, *9*, 504.
[12] L. Suo, Y.-S. Hu, H. Li, M. Armand, L. Chen, *Nat. Commun.* **2013**, *4*, 1481.

© 2018 WILEY-VCH Verlag GmbH & Co. KGaA, Weinheim

[13] R. Mogi, M. Inaba, S.-K. Jeong, Y. Iriyama, T. Abe, Z. Ogumi, *J. Electrochem. Soc.* **2002**, *149*, A1578.
[14] J. Qian, W. A. Henderson, W. Xu, P. Bhattacharya, M. Engelhard, O. Borodin, J.-G. Zhang, *Nat. Commun.* **2015**, *6*, 7362.
[15] J. Qian, B. D. Adams, J. Zheng, W. Xu, W. A. Henderson, J. Wang, M. E. Bowden, S. Xu, J. Hu, J. G. Zhang, *Adv. Funct. Mater.* **2016**, *26*, 7094.
[16] N. B. Aetukuri, S. Kitajima, E. Jung, L. E. Thompson, K. Virwani, M. L. Reich, M. Kunze, M. Schneider, W. Schmidbauer, W. W. Wilcke, *Adv. Energy Mater.* **2015**, *5*, 1500265.
[17] W. Zhou, S. Wang, Y. Li, S. Xin, A. Manthiram, J. B. Goodenough, *J. Am. Chem. Soc.* **2016**, *138*, 9385.
[18] K. K. Fu, Y. Gong, J. Dai, A. Gong, X. Han, Y. Yao, C. Wang, Y. Wang, Y. Chen, C. Yan, *Proc. Natl. Acad. Sci.* **2016**, *113*, 7094.
[19] G. Zheng, S. W. Lee, Z. Liang, H.-W. Lee, K. Yan, H. Yao, H. Wang, W. Li, S. Chu, Y. Cui, *Nat. Nanotechnol.* **2014**, *9*, 618.
[20] K. Yan, H.-W. Lee, T. Gao, G. Zheng, H. Yao, H. Wang, Z. Lu, Y. Zhou, Z. Liang, Z. Liu, *Nano Lett.* **2014**, *14*, 6016.
[21] C.-P. Yang, Y.-X. Yin, S.-F. Zhang, N.-W. Li, Y.-G. Guo, *Nat. Commun.* **2015**, *6*, 8058.
[22] L.-L. Lu, J. Ge, J.-N. Yang, S.-M. Chen, H.-B. Yao, F. Zhou, S.-H. Yu, *Nano Lett.* **2016**, *16*, 4431.
[23] Q. Yun, Y. B. He, W. Lv, Y. Zhao, B. Li, F. Kang, Q. H. Yang, *Adv. Mater.* **2016**, *28*, 6932.
[24] Q. Li, S. Zhu, Y. Lu, *Adv. Funct. Mater.* **2017**, *27*, 1606422.
[25] D. Lin, Y. Liu, Z. Liang, H.-W. Lee, J. Sun, H. Wang, K. Yan, J. Xie, Y. Cui, *Nat. Nanotechnol.* **2016**, *11*, 626.
[26] D. Lin, Y. Liu, Y. Cui, *Nat. Nanotechnol.* **2017**, *12*, 194.
[27] Z. Chen, W. Ren, L. Gao, B. Liu, S. Pei, H.-M. Cheng, *Nat. Mater.* **2011**, *10*, 424.
[28] S. Jin, Z. Sun, Y. Guo, Z. Qi, C. Guo, X. Kong, Y. Zhu, H. Ji, *Adv. Mater.* **2017**, *29*, 1700783.
[29] S. Jin, S. Xin, L. Wang, Z. Du, L. Cao, J. Chen, X. Kong, M. Gong, J. Lu, Y. Zhu, *Adv. Mater.* **2016**, *28*, 9094.
[30] Y. Guo, H. Li, T. Zhai, *Adv. Mater.* **2017**, *29*, 1700007.
[31] A.-R. O. Raji, R. Villegas Salvatierra, N. D. Kim, X. Fan, Y. Li, G. A. Silva, J. Sha, J. M. Tour, *ACS Nano* **2017**, *11*, 6362.
[32] C. Yang, Y. Yao, S. He, H. Xie, E. Hitz, L. Hu, *Adv. Mater.* **2017**, *29*, 1702714.
[33] H. Ye, S. Xin, Y.-X. Yin, J.-Y. Li, Y.-G. Guo, L. J. Wan, *J. Am. Chem. Soc.* **2017**, *139*, 5916.
[34] X. B. Cheng, T. Z. Hou, R. Zhang, H. J. Peng, C. Z. Zhao, J. Q. Huang, Q. Zhang, *Adv. Mater.* **2016**, *28*, 2888.
[35] R. Mukherjee, A. V. Thomas, D. Datta, E. Singh, J. Li, O. Eksik, V. B. Shenoy, N. Koratkar, *Nat. Commun.* **2014**, *5*, 3710.
[36] Y. Liu, D. Lin, Z. Liang, J. Zhao, K. Yan, Y. Cui, *Nat. Commun.* **2016**, *7*, 10992.
[37] Z. Liang, D. Lin, J. Zhao, Z. Lu, Y. Liu, C. Liu, Y. Lu, H. Wang, K. Yan, X. Tao, *Proc. Natl. Acad. Sci.* **2016**, *113*, 2862.
[38] S. S. Chi, Y. Liu, W. L. Song, L. Z. Fan, Q. Zhang, *Adv. Funct. Mater.* **2017**, *27*, 1700348.
[39] S. Liu, X. Xia, Y. Zhong, S. Deng, Z. Yao, L. Zhang, X. B. Cheng, X. Wang, Q. Zhang, J. Tu, *Adv. Energy Mater.* **2018**, *8*, 1702322.
[40] R. Zhang, X. R. Chen, X. Chen, X. B. Cheng, X. Q. Zhang, C. Yan, Q. Zhang, *Angew. Chem., Int. Ed.* **2017**, *56*, 7764.
[41] B. D. Adams, J. Zheng, X. Ren, W. Xu, J. G. Zhang, *Adv. Energy Mater.* **2018**, *8*, 1702097.
[42] C. Zhang, W. Lv, G. Zhou, Z. Huang, Y. Zhang, R. Lyu, H. Wu, Q. Yun, F. Kang, Q. H. Yang, *Adv. Energy Mater.* **2018**, 1703404.
[43] G. Bieker, M. Winter, P. Bieker, *Phys. Chem. Chem. Phys.* **2015**, *17*, 8670.

 © 2018 WILEY-VCH Verlag GmbH & Co. KGaA, Weinheim